IOP Publishing Metrologia

Metrologia **57** (2020) 025018 (7pp) https://doi.org/10.1088/1681-7575/ab63af

# Robust phase-stepping interferometry for traceable length measurements in a Hilger–Watts gauge-block interferometer

**Ian D Leroux and Brian J Eves**

National Research Council Canada, K1A 0R6 Ottawa, Ontario, Canada

E-mail: Ian.Leroux@nrc-cnrc.gc.ca

Received 4 November 2019, revised 6 December 2019
Accepted for publication 18 December 2019
Published 19 March 2020

**Abstract**

We demonstrate a simple adaptation of the venerable Hilger–Watts gauge-block interferometer capable of performing automated, traceable calibrations of gauge block length by phase-stepping interferometry (PSI). We discuss the selection of robust PSI filtering algorithms to counteract in software the flaws of the hardware implementation, including markedly non-sinusoidal fringes and inhomogeneous phase step size. We find that the length measurement errors attributable to the phase measurement can be reduced to 0.6 nm, even with a simple retrofit to an instrument not originally designed for PSI.

Keywords: gauge blocks, interferometry, phase-stepping interferometry, Hilger–Watts interferometer

(Some figures may appear in colour only in the online journal)

## 1. Background

The central task in an interferometric measurement of length is to estimate the phase representing the path-length difference to be measured. When the path-length difference varies across an image, phases can be estimated from the spatial position of the resulting interference fringes. Such estimates require only a single interferogram and can be performed by a trained human operator without electronic assistance. However, once it became possible to record interferograms electronically, it was soon recognized that stepping or scanning the path-length difference and recording the interference intensity several times at a given spatial position offered several advantages [1, 2]. Such phase-stepping interferometry (PSI) is easy to automate because the data-taking requires no operator judgment or image processing [1], is insensitive to spatial intensity gradients in the image since the phase can be assessed independently at each position, and generalizes straightforwardly to the measurement of 2D phase maps for assessing surface form [3].

PSI works best with perfectly sinusoidal interference fringes and known, uniform step sizes. When designing a new instrument, careful engineering can ensure that only two optical paths interfere, that the detector response is linear—keeping the fringes sinusoidal—and that the phase steps are uniform and accurate [4]. However, when refitting and automating older interferometers [5, 6], the optical design of the original instrument may make it impractical to achieve ideal phase-stepping behaviour. Such instruments can benefit from numerical techniques developed for automated inspection of optical surfaces [3], where the use of Fizeau interferometers leads to non-sinusoidal fringes [7] and where high numerical apertures lead to inhomogeneous phase step sizes [8]. Here we describe our experience with this approach while modernizing a Hilger–Watts gauge-block interferometer.

We are not the first to use PSI in a Hilger–Watts interferometer, but the only previous implementation of which we are aware, that of [9], is based on sweeping the wavelength of the illuminating laser. While this is now the recommended phase-stepping method in surface-inspection applications [10], it is ill-suited to gauge-block length measurements which involve the simultaneous measurement of two different optical paths (one for each end of the gauge) whose phases vary differently with wavelength. It is also challenging, when sweeping the wavelength, to maintain a suitably low wavelength uncertainty for measuring distances of several cm. Accordingly, [9] describes the use of PSI only for tests of form and parallelism

 

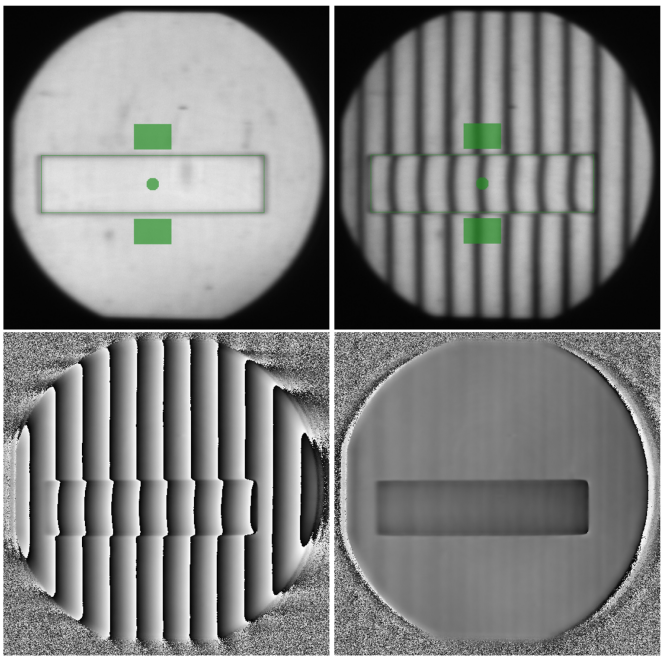

**Figure 1.** Upper left: Camera view under incoherent lighting, showing the automatically-determined block position. The green dot marks the gauging point and the two filled green rectangles mark the regions of the platen used to establish the reference plane. Upper right: Same view under laser illumination, showing interference fringes aligned for measurement. A series of such images are recorded, displacing the flat to shift the fringes for each image. Lower left: Resulting phase map. Lower right: Phase map after unwrapping and removing an overall tilt. The greyscale for both phase maps covers a full fringe, or 272 nm.

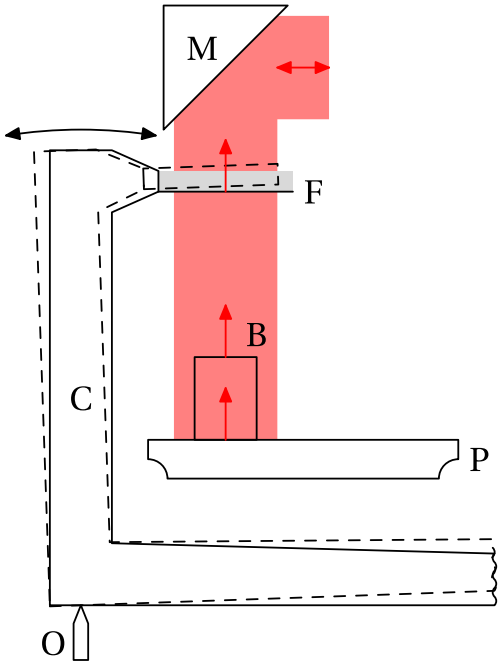


**Figure 2.** Layout of the key components of the modified Hilger–Watts interferometer. A collimated horizontal light beam is deflected downward by a 45° mirror M, goes through an optical flat F whose coated lower face reflects a reference wavefront, and then illuminates a gauge-block B wrung to a rotating platen P. Reflections from the flat, block, and platen travel back up the beam to the imaging optics (not shown). The optical flat is mounted to a tilting column C, allowing fine adjustment of its angle with respect to the platen (as indicated by the curved black arrows). As the pivot point O for the column is outside the beam, angular adjustments also displace the optical flat along the beam.

of the gauging faces, whereas calibration of the gauge block length is still determined from spatial fringe offsets [6].

The system we describe here uses fixed-frequency light sources and PSI for gauge block length measurements. No additional hardware is needed for phase-stepping and the data-processing required to extract the phase at each pixel is simple addition and multiplication by fixed constants, with no need for heuristics to distinguish interference fringes from other lines in the image and with no ambiguity as to whether heights are increasing or decreasing from one fringe to the next. A single measurement produces the phase needed for length calculations, a height map useful for assessments of form errors [9, 11], and a vectorial estimate of the angle between the optical flat and the surfaces beneath it. The fact that a single easily-implemented PSI measurement can simultaneously provide the information needed for length calculations, assessments of surface form, and automatic realignment of the optical flat and interference fringes in unsupervised operation, makes this an attractive approach for upgrading widely-deployed but elderly instruments such as the Hilger–Watts.

## 2. Apparatus

The Hilger–Watts interferometer, designed in the 1930s at NPL [12] and commercially available into the 1960s, is still used in some laboratories for the interferometric calibration of gauge blocks. Although originally designed for completely manual operation, with Cd and Hg discharge lamps as the wavelength standards, several of these instruments have been updated to use laser sources and to automate the estimation of fringe positions [5, 6]. We have undertaken a similar modernization, using HeNe lasers at 633 nm and 544 nm as the wavelength standards, adding a spinning diffuser to suppress the transverse coherence of the laser beam and the resulting diffraction rings, motorizing the operator controls, and mounting a camera to the former eyepiece. The resulting system operates unattended, measuring as many blocks as can be wrung to its rotating platen (typically around 12, but up to 18 with care [12]). Each block in turn is automatically positioned in the measurement beam aperture (figure 1 upper left). PSI-derived height maps are then used to align the interference fringes (figure 1 upper right), map the surfaces of the block and platen (figure 1 lower phase maps), and extract the phase differences for each laser corresponding to the block length. The reliability of this automatic operation comes in part from the determinism and robustness of PSI.

To allow straightforwardly-traceable PSI-based length measurement, we need to vary the optical path length difference between interfering beams while maintaining a known wavelength. Figure 2 is a schematic depiction of the relevant portion of the instrument. Light travelling downward toward

the gauge block first crosses an optical flat (F) whose coated lower surface reflects a portion of the beam as a reference wavefront. The transmitted portion is reflected by the platen (P) and gauge block (B). The optical flat is mounted to a tilting column (C), which is used to align the flat quasi-parallel with the platen. A deliberate misalignment of 60 µrad introduces the fringe pattern seen in the upper-right image of figure 1. Crucially, the pivot point for the tilting column lies ≈ 70 mm away from the beam axis, so small angular adjustments also raise and lower the optical flat, changing the distance between flat and platen by ≈ 70 nm/µrad. The angle of the column is controlled by a fine-pitch screw at the end of a 0.8 m lever arm. A servo-motor driving this screw through a reduction gearbox can thus step the phase. This system requires no additional hardware beyond what would already be necessary to automate the optical flat alignment, and is free of the non-linear displacement errors often seen in solid-state phase shifters using piezo-electric actuators or liquid-crystal modulators [13]. On the other hand, it introduces a large spatial inhomogeneity in the phase steps: for a given angular step of the column, the vertical displacement of the flat varies by ≈ ± 30% depending on the distance from each portion of the beam to the column's axis of rotation (O).

Note that, as seen in figure 2, the same motion that raises and lowers the flat along the beam also traverses it across the beam. A typical PSI scan requiring a ~600 nm displacement along the beam leads to an undesired transverse displacement of ~1.7 µm. However, while the relevant scale for vertical displacements is the optical wavelength, that for transverse displacements is the resolution of the camera images, which is diffraction-limited to hundreds of micrometers. Thus, while the transverse displacements are larger in absolute terms, their effect on the recorded camera images is negligible.

The upper graph of figure 3 shows intensity values at a single camera pixel, taken from 96 images recorded at intervals of 1/16 of a fringe. Camera data is averaged for 200 ms for each point, to average out a vibration in the frame of the interferometer. The markedly non-sinusoidal character of the fringes is a consequence of the basic optical design of the Hilger–Watts interferometer: the space between the optical flat and the platen forms a planar Fabry–Pérot cavity like that of a Fizeau interferometer, and multiple reflections between the surfaces are unavoidable. We therefore fit the fringes to a model of the form

$$I(t) = (A_0 + A_1\omega t)\left(1 - \frac{B}{1 - C\cos(\omega t + \phi_0)}\right). \qquad (1)$$

This is a slight modification of the Airy formula used for Fizeau interferometers [14–16], with an additional allowance for linear intensity drift. Here $t$ labels camera frames and is interpreted as a time in units of phase steps, $\omega$ is the size of a phase step and thus the fringe frequency in rad/step, and $\phi_0$ represents the phase of the fringe at $t = 0$. $A_0$ and $A_1$ corresponds to the incident intensity and its drift, while

$$B = \frac{(1 - r_1^2)(1 - r_2^2)}{1 + r_1^2 r_2^2} \quad \text{and} \quad C = \frac{2r_1 r_2}{1 + r_1^2 r_2^2} \qquad (2)$$

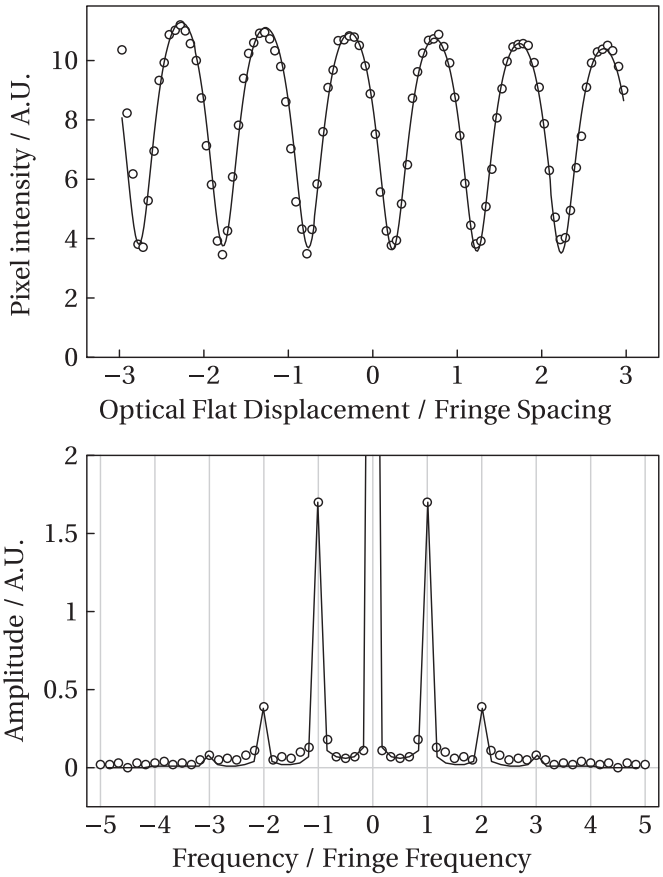


**Figure 3.** Above: Interferogram recorded at a single image pixel while moving the optical reference flat through 3 wavelengths of the 544 nm laser. Solid line shows a fit to a Fizeau fringe as described in the text. Below: Corresponding Fourier amplitude spectra.

depend on the reflections coefficients $r_1$ and $r_2$ of the two surfaces forming the cavity and together determine the visibility and form of the fringes.

Taking the Fourier transform of the interferogram (data and fit) yields the amplitude spectra shown in the lower graph of figure 3. To either side of the DC peak corresponding to the average intensity, we see the fundamental fringe oscillation (± 1 on the graph's abscissa), followed by the higher harmonics associated with the deformation of the fringe. The amplitude ratio between successive harmonics, which corresponds to the geometric mean of the reflectances of the optical flat and platen [16], is $r_1 r_2 = (1 - \sqrt{1 - C^2})/C = 0.22$. The second and third harmonics, with amplitudes 22% and 5% of the fundamental, are clearly visible in the spectrum.

## 3. PSI algorithm design

The higher harmonics in the interferogram make it unusable for the 4-frame Carré algorithm traditionally employed in gauge-block interferometers [2, 17]. That algorithm, designed for the sinusoidal fringes of Twyman-Green interferometers, produces half-radian (~25 nm) phase errors and even unphysical imaginary phase solutions when applied to the distorted fringe of this instrument. A PSI algorithm intended specifically

for Fizeau interferometers, accounting for harmonics of all orders, has been known for three decades [14–16], but it is numerically ill-behaved in the presence of step-size errors and can give divergent results at certain phases [15]. Because of the spatially inhomogeneous step size in our PSI implementation, we need a more robust PSI algorithm.

A variety of general formalisms, differing in their mathematical approach and suitable for different classes of experimental imperfections, have been used to design and analyze robust PSI algorithms [13, 18–21]. Since we are concerned with non-sinusoidal fringes and spatially inhomogenous step sizes, but not time-varying step sizes (frequency chirp), we use essentially the same framekwork as Surrel [20]. Consider a general periodic intensity function

$$I(t) = \sum_{m=-\infty}^{\infty} \alpha_m \mathrm{e}^{\mathrm{i}m\omega t}, \tag{3}$$

where $m$ labels the harmonics and $\alpha_m = \alpha^*_{-m}$ are their complex Fourier amplitudes. The phase to be measured is the complex argument of the amplitude $\alpha_1$ and a PSI algorithm can be understood as a filter intended to isolate this amplitude. Conventional PSI algorithms involve a linear combination of regularly-spaced intensity readings

$$S = \sum_{t=0}^{M-1} c_t I(t). \tag{4}$$

Decomposing the complex coefficients $c_t$ into real and imaginary parts, we can interpret this as a pair of real-valued filters for the quadratures of the signal:

$$S = X + \mathrm{i}Y \tag{5}$$

$$X = \sum_{t=0}^{M-1} \Re(c_t) I(t) \quad Y = \sum_{t=0}^{M-1} \Im(c_t) I(t) \tag{6}$$

The phase is estimated as the complex argument of the filtered signal $S$

$$\phi = \arg(S) = \arctan\left(\frac{Y}{X}\right). \tag{7}$$

Thus, calculating the phase at runtime is a simple matter of multiplying the intensities in the different readings by known constants, adding up the results to obtain the quadrature signals $X$ and $Y$, and converting the result from Cartesian to polar coordinates. The harder problem, which must be solved in advance, is to choose a good set of coefficients $c_t$.

Surrel pointed out that it is convenient to combine the coefficients into a characteristic polynomial

$$P(z) = \sum_{t=0}^{M-1} c_t z^t, \tag{8}$$

in terms of which equations (3) and (4) can be combined as

$$S = \sum_{t=0}^{M-1} c_t \sum_{m=-\infty}^{\infty} \alpha_m \mathrm{e}^{\mathrm{i}m\omega t} = \sum_{m=-\infty}^{\infty} \alpha_m P\left(\mathrm{e}^{\mathrm{i}m\omega}\right). \tag{9}$$

The design of the filter reduces to choosing the roots of $P$. Alternatively, following Servin *et al* [21], one can treat $H(-\omega) = P\left(\mathrm{e}^{\mathrm{i}m\omega}\right)$ as the Fourier spectrum of the filter and design this spectrum as a product of sinusoidal factors, whose time-domain representations correspond to regularly spaced samples of $I(t)$. The polynomial approach simplifies filter synthesis and algebraic manipulation, while the spectrum is convenient for visualizing the effects of filter design choices.

A useful filter must, at a minimum, suppress the DC offset $\alpha_0$ and the counter-rotating amplitude $\alpha_{-1}$, so $P$ should have roots at 0 and $\mathrm{e}^{-\mathrm{i}\omega}$. Additional roots can suppress higher-order harmonics $\alpha_{\pm m}$, if the fringes are non-sinusoidal, or extend the range of step sizes $\omega$ for which the suppression of undesired components is effective.

As a starting point, we consider the 9-frame broadband filter described by Servin *et al* [21], which has recently been adopted for use in gauge-block interferometers at NRC and MIKES [22]. Designed for a sinusoidal fringe with a nominal step size $\omega_0 = \pi/2$, it uses a single root at $z = \mathrm{e}^{\mathrm{i}0}$ to suppress the DC component, and double roots at $z = \mathrm{e}^{-\mathrm{i}\pi/4}, \mathrm{e}^{-\mathrm{i}\pi/2}$, and $\mathrm{e}^{-\mathrm{i}3\pi/4}$ to suppress the counter-rotating $\alpha_{-1}$ component even in the presence of large step-size errors (60% or more). However, the $\alpha_{\pm 2}$ harmonics are suppressed only by a single root at $z = \mathrm{e}^{\mathrm{i}\pi}$, meaning that they leak through the filter as soon as $\omega$ differs from $\pi/2$. The $\alpha_{-3}$ harmonic is not suppressed at all, being indistinguishable from the $\alpha_1$ signal due to Nyquist aliasing (see figure 4, top).

The fixed frequency response of linear PSI filters limits the achievable robustness to step-size errors when the second harmonic is significant [10]. Consider a 50% reduction in step size which tunes the second harmonic to the same frequency $2\omega = \omega_0$ as the design frequency for the fundamental signal. Any filter which successfully suppressed the former would also suppress the latter, and one cannot broaden the stopband for $\alpha_2$ without restricting the passband for $\alpha_1$. The allowable step-size errors being thus limited, we should invest effort in suppressing higher harmonics for modest step-size errors rather than aiming for broad bandwidth. This leads us to consider a PSI algorithm which Surrel calls WDFT [20, 23], otherwise known as Surrel's $2N-1$ algorithm [24, 25]. For a design step size $\omega_0 = 2\pi/N$, the corresponding characteristic polynomial $P$ has double roots at all but one of the $N$th roots of unity, and suppresses harmonics out to $\alpha_{\pm(N-2)}$. Because all roots are doubled, so that the spectral response approaches zero quadratically near all undesired frequency components, the filter is linearly insensitive to small step-size errors. The double root at 1 (DC) makes it insensitive to linear intensity drift. Surrel's $2N-1$ is the minimal PSI algorithm combining robustness to harmonics up to a given order, to step size errors, and to linear intensity drift [23]. The time domain coefficients $c_t$ for this filter are those of a discrete Fourier transform with a triangular windowing function.

The lower three graphs of figure 4 show the spectra for three instances of Surrel's $2N-1$ with $N = 5, 6, 7$. The first of

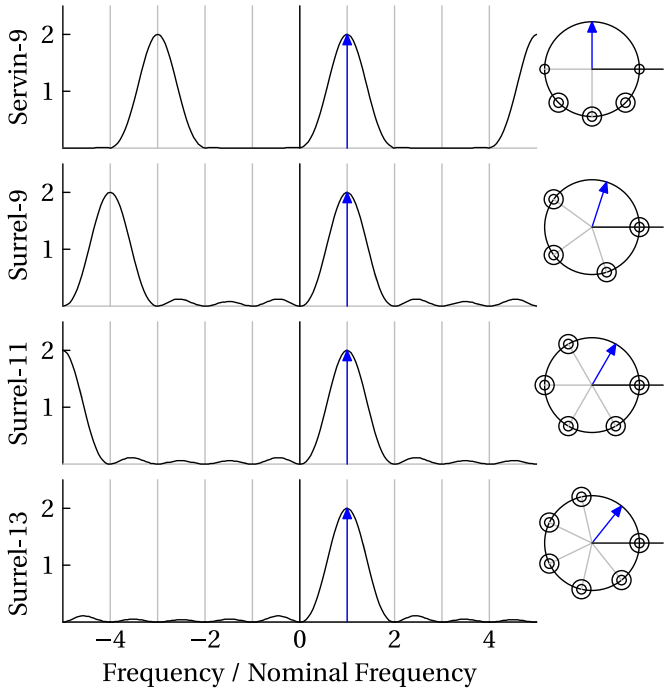


**Figure 4.** Fourier amplitude spectra [21] (left) and characteristic diagrams [20] (right) for four PSI algorithms tested in this work. The DC or background signal is indicated by a black line. Blue arrows mark the nominal carrier frequency to be detected. Grey lines indicate the other harmonics of the nominal frequency. In the characteristic diagrams, a small circle represents a single root (a simple zero of the filter spectrum) while a pair of concentric circles represents a double root (a second-order zero of the filter spectrum). From the top, the four algorithm's are Servin's 9-frame broadband algorithm [21] and Surrel's $2N-1$ algorithm [20] with 9, 11, and 13 frames.

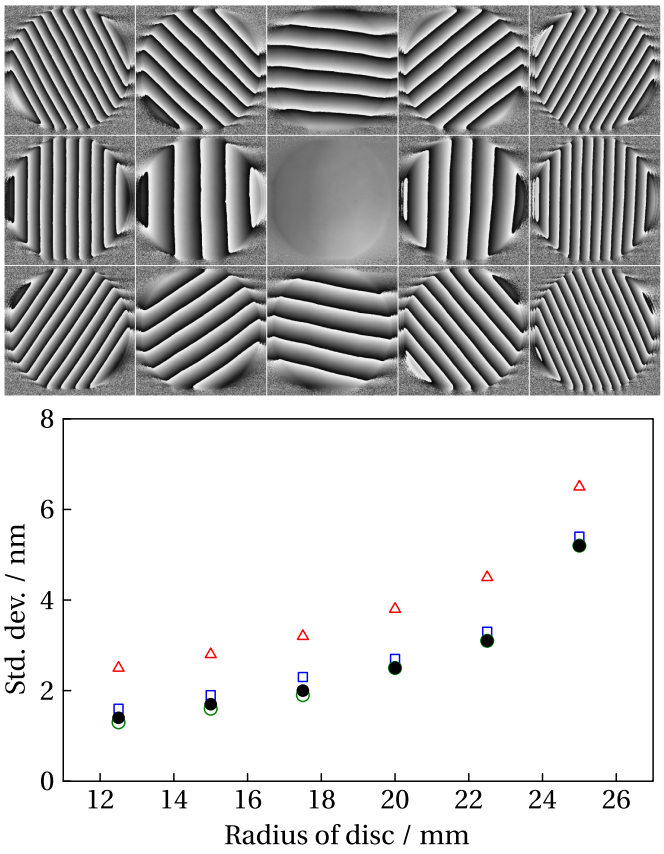


**Figure 5.** Above: 15 phase maps of the same platen surface at different angles of the reference flat. After unwrapping and removing global tilts and offsets, these maps describe the same surface and the discrepancies between them are a measure of errors (including periodic errors) in the PSI system. Below: Standard deviation between maps as a function of the radius of the region over which they are compared, for Servin's 9-frame algorithm (red triangles) and Surrel's $2N-1$ algorithm with 9 frames (blue squares), 11 frames (black filled circles), and 13 frames (green open circles).

these, which uses 9 frames like Servin's filter, yields poorer suppression of the counter-rotating $\alpha_{-1}$ component far away from the design frequency (more ripple in the stopband), but suppresses the second and third harmonics which Servin's filter does poorly or not at all. Increasing the number of frames successively suppresses the fourth and fifth harmonics, and has the secondary benefit of reducing the residual sensitivity between the lower harmonics.

## 4. Phase-mapping performance

To assess the performance of our implementation of these PSI algorithms, we compare an ensemble of phase maps of a static platen. If the measurements were perfect, the phase maps would differ only by rigid-body rotations due to alignment changes of the flat. To ensure that periodic errors due to the multi-beam interference are detected in the comparison, we tilt the flat differently for each map (in increments of ca. 30 µrad) to change the fringe patterns. An example set of 15 phase maps (before unwrapping) is shown at the top of figure 5. Unwrapping, removing global tilts and offsets, taking the standard deviations of the phases across maps, and pooling them over all pixels in some region gives an estimate of the single-pixel errors in the phase maps. The results depend on the size of the region used for the analysis: larger regions include greater spatial variations in the step size and are eventually affected by diffraction artifacts at the edge of the beam. We use a circular disc centred in the beam as the analysis region, and plot the result as a function of increasing disc radius in the lower half of figure 5. We see a marked improvement in the consistency of the maps when going from Servin's 9-frame filter (red triangles) to Surrel's 9-frame filter (blue squares), thus suppressing the second and third harmonics in the spectrum. Suppressing the fourth harmonic with 11 frames (black filled circles) has a modest effect, but going further, to 13 frames (green open circles), brings no further benefit beyond the averaging of random noise to be expected from the additional data. Since the fifth harmonic is expected to have an amplitude only 0.2% that of the carrier, this is unsurprising.

Qualitatively, all four of the filters encounter a similar limitation at the left edge of the beam, close to the pivot point, where the step size is reduced and the $\alpha_2$ harmonic shifts down into the filter passband intended for the $\alpha_1$ signal. This is visible as a coarse ripple in the lower-right phase map of figure 1. Servin's 9-step filter fares particularly poorly at the right side of the beam, because the $\alpha_{-2}$ harmonic shifts into the aliased passband at $\alpha_{-3}$ and is no longer suppressed.

In practice we use Surrel's $2N-1$ with $N=6$, i.e. 11 frames, and it is instructive to contrast this choice with that of the wavelength-scanning PSI implementation of [9]. Because their wavelength-tuning system involved a piezo with a slightly non-linear response, they used an 11-frame filter designed to be robust to non-linear (i.e. chirped) phase shifts [13, 26]. With a step size of $\omega_0 = 2\pi/5$, this filter is robust to harmonics out to $\alpha_{\pm 3}$. While our system suffers from greater spatial inhomogeneity of the step size, temporal chirp is not a concern for us and so we sacrifice chirp-resistance to suppress an additional order of harmonics with the same number of frames. The performance of the two systems, designed for different purposes, is not directly comparable, but we note that the $0.005\lambda$ resolution claimed for their system would correspond to $\approx 3$ nm in ours, which is the single-pixel standard deviation we obtain over the whole usable beam (figure 5, black circles, 22.5 mm radius). Thus, with PSI filters chosen to match their respective instrumental limitations, the two systems perform similarly.

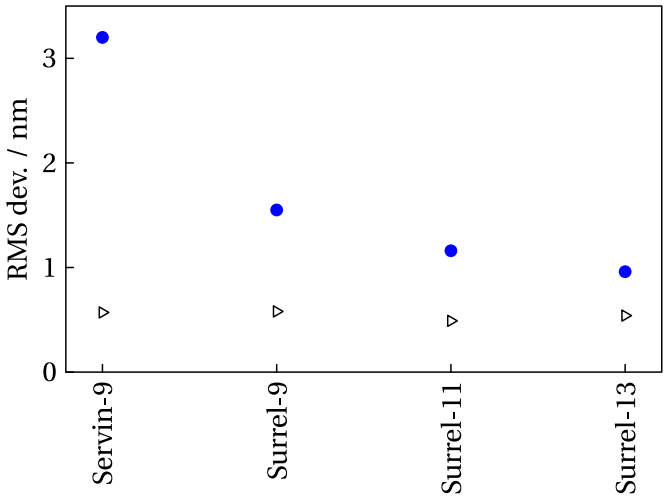


**Figure 6.** RMS errors attributable to PSI for gauge-block length measurements with each of four PSI filters. Filled blue circles: with optical flat parallel to platen. Open black triangles: with optical flat tilted by 60 μrad relative to platen.

## 5. Length-measurement performance

We have used each of the PSI algorithms of figure 4 to perform 104 length measurements on 13 gauge blocks with nominal lengths ranging from 1 mm to 40 mm, where each measurement involves two separate readings collected at 633 nm and 544 nm. Because the phases measured at the two wavelengths differ, they are affected differently by periodic phase-estimation errors. Discrepancies between the lengths obtained from the two readings are thus sensitive to systematic phase estimation errors as well as to random measurement noise. Pooling these discrepancies across all blocks and measurements thus yields an estimate of the uncertainty attributable to the PSI reading.

The blue circles in figure 6 show the RMS block-length error attributable to a single PSI reading when the optical flat is kept parallel to the platen, the so-called 'flat fringe' or 'fluffed-out fringe' condition. In this case the interference phase is roughly constant across the platen and, with a different phase, across the gauging face. The residual phase-dependent non-linear errors thus appear as uncorrelated but global errors on the platen and gauging face heights. PSI filters which suppress these errors more effectively reduce the block-length noise, which falls from 3 nm when using Servin's 9-frame algorithm to 1 nm when using Surrel's $2N-1$ with 13 frames. If the optical flat is deliberately tilted by 60 μrad to introduce a phase gradient across the image, one obtains a fringe pattern like the one of figure 1. Phase-dependent errors now vary periodically across the image. If a sufficiently large area is used to fit the reference plane to the platen surface, this periodic variation can be averaged out by the plane fit, reducing the sensitivity to non-linear errors. In this configuration (black triangles in figure 6), the RMS block-length noise falls to 0.6 nm for all four filters tested here. In practice it is easy to combine both approaches, choosing a filter with low residual non-linear errors and tilting the optical flat to reduce sensitivity to those errors. The resulting phase estimation errors of 0.01 rad or 0.2% of a fringe for a single reading are an order of magnitude better than could be achieved by visual estimation of fringe offsets in the original instrument.

Note that even NMI-level length calibrations of short gauge blocks rarely have total standard uncertainties much below 10 nm [27], so the phase measurement noise is far from dominating the final measurement uncertainty for gauge block length. The low noise of the PSI system's readings does, however, reduce the chance of blunders when choosing integer fringe orders by the method of exact fractions, and thus recovers some of the robustness and reliability lost by replacing the 4 – 6 measurement wavelengths of the original Hilger–Watts instrument's discharge lamps by only two lasers. The reduced noise also corresponds to improved short- and medium-term repeatability, which is valuable both when investigating potential sources of error that might otherwise be masked by measurement noise and when monitoring the performance of the instrument using process-control measurements on check gauges.

## 6. Outlook

We have shown that even a simple phase-stepping system with obvious imperfections suffices for state-of-the-art calibrations of gauge block length, provided that suitable PSI filters are employed. Servin's broadband 9-step filter performs adequately for length measurements, provided that care is taken to tilt the reference plane and average over periodic errors due to multi-path interference. Surrel's $2N-1$ filter, which is explicitly designed for non-sinusoidal signals and better-suited to the particular imperfections of our apparatus, yields phase maps with reduced periodic errors. The improved quality of the phase maps would be helpful for automatic assessment of the deviation from flatness and variation in length of the gauge blocks as specified in ISO 3650 [9, 11]. Even for simple measurements of central length, however, we

find that better phase maps are valuable because they relax the requirements on optical flat alignment while simultaneously allowing more accurate automatic determination of the alignment. They also allow a more stringent automatic validation of the measurement results, by reducing the expected deviation from flatness of the measured platen surface. Together, all these small advantages make for a more reliable instrument, one which can perform many hundreds of unsupervised gauge-block measurements without a fault or blunder.

If even higher-quality phaseenlargethispage-100pt maps were needed, for instance if the instrument were to be adapted for surface-flatness assessments, a number of improvements could be made with no hardware changes. The simplest would be to use triple or even quadruple roots instead of the double roots of Surrel's $2N-1$ algorithm. Such $3N-2$ [24] and $4N-3$ [25] filters provide cubic or quartic suppression of the spectral leakage due to small step-size errors, and have been shown to reduce errors in optics-inspection applications [28]. If computational cost is no object, an iterative least-squares fit of a parametric model of the instrument imperfections [29, 30] can be used instead of a traditional PSI algorithm. This avoids altogether the limitations of a linear filter with a fixed frequency response, but the convergence of the fit depends on initial estimates of model parameters and of the phase map. While we prefer the simplicity and determinism of conventional PSI for automation purposes, a final reanalysis of the collected data by an iterative fit might improve precision in some cases.

## Acknowledgment

We thank Rui Zhao for assistance with the measurements and the Air Force Metrology and Calibration (AFMETCAL) program of the United States Air Force for the loan of a Hilger–Watts interferometer.

## References

[1] Terrien J 1959 *Opt. Acta* **6** 301
[2] Carré P 1966 *Metrologia* **2** 13
[3] Bruning J H, Herriott D R, Gallagher J E, Rosenfeld D P, White A D and Brangaccio D J 1974 *Appl. Opt.* **13** 2693
[4] Schödel R, Nicolaus A and Bönsch G 2002 *Appl. Opt.* **41** 55
[5] Howick E F, Watkins L and Tan S M 2003 *Metrologia* **40** 139
[6] O'Hora M, Bowe B, Toal V and Peyton S 2005 *Opt. Eng.* **44** 035601
[7] Hariharan P 1987 *Appl. Opt.* **26** 2506
[8] Creath K and Hariharan P 1994 *Appl. Opt.* **33** 24
[9] O'Hora M, Bowe B and Toal V 2006 *Appl. Opt.* **45** 5607
[10] de Groot P J 2014 *Appl. Opt.* **53** 4334
[11] ISO 3650:1998 1998 Geometrical Product Specifications—Length standards—Gauge blocks (Geneva: Int. Organization for Standardization)
[12] Rolt F H 1957 *Metrology of Gage Blocks* NBS Circular No. 581 (Washington D.C.: National Bureau of Standards) pp 27–41
[13] Hibino K, Oreb B F, Farrant D I and Larkin K G 1997 *J. Opt. Soc. Am.* A **14** 918
[14] Bönsch G and Böhme H 1989 *Optik* **82** 161
[15] Nicolaus R A 1993 *Appl. Opt.* **32** 6380
[16] Dorrío B V, Blanco-García J, López C, Doval A F, Soto R, Fernández J L and Pérez-Amor M 1996 *Appl. Opt.* **35** 61
[17] Bönsch G 2001 *Recent Developments in Traceable Dimensional Measurements* 4401, ed Decker J E and Brown N (Bellingham, WA: SPIE) pp 1–10.
[18] Freischlad K and Koliopoulos C L 1990 *J Opt. Soc. Am.* A **7** 542
[19] Hibino K, Oreb B F, Farrant D I and Larkin K G 1995 *J. Opt. Soc. Am.* A **12** 761
[20] Surrel Y, 1996 *Appl. Opt.* **35** 51
[21] Servin M, Estrada J C and Quiroga J A 2009 *Opt. Express* **17** 21867
[22] Byman V and Lassila A 2015 *Meas. Sci. Technol.* **26** 084009
[23] Surrel Y, 1997 *Appl. Opt.* **36** 805
[24] Kim Y, Hibino K, Sugito N and Mitsuishi M 2014 *Opt. Express* **22** 18203
[25] Kim Y, Hibino K, Hanayama R, Sugito N, Mitsuishi M 2014 *Opt. Express* **22** 21145
[26] Hibino K 1999 *J. Opt. Rev.* **6** 529
[27] BIPM 2020 KCDB (https://www.bipm.org/kcdb/)
[28] Kim Y, Hibino K, Sugito N and Mitsuishi M 2015 *Appl. Opt.* **54** 4207
[29] Deck L L 2014 *Appl. Opt.* **53** 4628
[30] Kihm H 2016 *Opt. Eng.* **55** 074101